Early and persistent supershear rupture of the 2018 Mw 7.5 Palu earthquake

Han Bao[1], Jean-Paul Ampuero[2,3], Lingsen Meng*[1], Eric J. Fielding[4], Cunren Liang[3], Tian Feng[1], Hui Huang[1]

1. Earth, Planetary and Space Sciences, University of California, Los Angeles, USA
2. Université Côte d'Azur, IRD, CNRS, Observatoire de la Côte d'Azur, Géoazur, France
3. California Institute of Technology, Seismological Laboratory, USA
4. Jet Propulsion Laboratory, California Institute of Technology, USA

*Corresponding author. Tel.: +1 310 825 1885.
E-mail address:meng@ess.ucla.edu (L. Meng).

Key points
- The rupture speed of the 2018 Palu earthquake is supershear *from very early on*.
- Yet rupture is not as fast as P waves, it is an unstable-supershear speed (slower than the Eshelby speed)
- This observation is enabled by slowness-enhanced back-projection
- Supershear is persistent despite complexities of fault geometry revealed by remote sensing

Abstract

Supershear earthquakes with rupture velocity exceeding shear-wave speeds, previously observed in laboratory experiments and large strike-slip events, often have an initial sub-shear stage before they transition to supershear. In this study, integrated geophysical observations of the 2018 Mw 7.5 Palu, Indonesia earthquake, provide robust evidence of an early and persistent supershear rupture speed. Slowness-enhanced back-projection (SEBP) of teleseismic data provides a sharp image of the rupture process, consistently across multiple arrays. The inferred rupture path agrees with the surface rupture trace inferred from the net surface displacement field derived by sub-pixel InSAR image correlation. The SEBP results indicate a sustained rupture velocity of 4.1 km/s from the rupture initiation to the end, despite large fault bends. The persistent supershear speed is further validated by evidence of far-field Rayleigh Mach waves in regional seismograms. The short or absent supershear transition distance can be caused by high initial shear stress or short critical slip-weakening distance, and promoted by fault roughness near the hypocenter. Steady rupture propagation at a supershear speed considered to be unstable, lower than the Eshelby speed, could result from the presence of a damaged fault zone.

Introduction

The speed at which an earthquake rupture propagates affects its energy balance and the severity of its radiated ground shaking. While most earthquakes rupture at speeds lower than shear wave velocity, faster, so-called supershear earthquakes have been predicted by theory and simulations (Burridge 1973; Andrews 1976) and observed in laboratory experiments (e.g. Xia et al, 2004) and large strike-slip earthquakes (e.g. Das 2015). Whether observable fault properties control the occurrence of supershear rupture in nature is not completely understood. Supershear ruptures have been proposed to occur on smooth and straight faults (Bouchon et al. 2010), and to be promoted on fault segments with well-developed damage zones (Huang et al., 2015; Perrin et al., 2016) and on geometrically rough faults (Bruhat et al., 2016).

On 28 September 2018, an earthquake with moment magnitude Mw 7.5 occurred in Sulawesi, Indonesia (Fig. 1), with epicentre located about 80 km north of the city of Palu. The earthquake ruptured along the Palu-Koro fault, a strike-slip left-lateral fault with a geodetic slip rate of 42 mm/year (Socquet et al., 2006), a record of large earthquakes (with magnitudes from 7 to 8, Watkinson and Hall, 2017) and previously identified seismic hazard (Cipta et al., 2016). This event triggered damaging tsunami and landslides causing more than 2,000 casualties.

Here we focus on a feature of this earthquake that is important for our fundamental understanding of earthquake physics. We present robust seismological evidence of an early and persistent supershear rupture, propagating steadily at a speed that is thought to be unstable. We further exploit remote sensing observations of the rupture trace geometry to discuss possible relations between supershear rupture and fault structure, especially in light of recent theoretical results on the role of geometrical fault roughness and damaged fault zones on supershear rupture.

Remote sensing observations of the surface rupture

Synthetic aperture radar (SAR) analysis provides key constraints on the Palu earthquake rupture geometry. To measure the net surface deformation due to the earthquake, we processed data from the Japan Aerospace Exploration Agency (JAXA) Advanced Land Observation Satellite-2 (ALOS-2) Phased-Array L-band Synthetic Aperture Radar-2 (PALSAR-2) instrument. We extracted along-track displacements in the ALOS-2 satellite track direction (azimuth -11.7° from north) using pixel offset tracking or sub-pixel image correlation (e.g., Pathier et al., 2006) with the InSAR Scientific Computing Environment (ISCE) software (Rosen et al., 2012). We analyzed PALSAR-2 images acquired in the fine-beam mode (approximately 4 m pixel spacing) on ascending paths 126 and 127 by precisely mosacking the frames (Liang and Fielding, 2017) before the pixel offset tracking, using 128 by 128 pixel matching windows (see Fig. 1). Data used is listed in Table S1.

The inferred surface rupture reveals major geometrical complexities and differences between northern and southern portions (Figs. 1a and S1). The satellite tracks are very close to anti-parallel to the strike of the rupture, so the along-track displacements are almost parallel to the fault strike and show the location of the surface rupture on land where the east side moved north (positive in Fig. 1) and the west side moved south. No surface rupture is discerned north

2

of the epicenter. The southern end of the surface rupture is at 119.99°E, 1.47°S. The northern part of the rupture, from the epicenter to its intersection with the Palu Bay coast at 119.83°E, 0.69°S, is less straight than the rupture from Palu city to the south. There is a substantial right-bend in the rupture at 119.83°E, 0.34°S, over which the fault trace is offset by about 4 km in the direction perpendicular to the main rupture strike. The rupture from Palu city to the south is very straight until it makes a large left-bend at 119.885°E, 1.185°S. The left-bend is about 8.5 km along the diagonal and 6.5 km perpendicular to the main fault strike. The slip is smaller south of the bend and decreases gradually to the end.

Supershear rupture processes imaged by slowness-enhanced back-projection

Owing to the advent of regional dense seismic arrays, teleseismic back-projection (BP) rupture imaging has become one of the essential techniques to constrain the kinematic rupture properties of large earthquakes, including rupture length, direction, speed and segmentation (e.g. Kiser & Ishii, 2017). Without prior knowledge of fault geometry or rupture speed, BP determines the location, timing and relative power of coherent high-frequency sources by exploiting the coherency of seismic waveforms across dense arrays. Here, to achieve high resolution rupture imaging, we apply the Multitaper-MUSIC array processing technique (Meng et al., 2011), which can resolve closer simultaneous sources and is less sensitive to aliasing than conventional BP techniques. The "reference window" strategy (Meng et al., 2012) is also applied to eliminate the "swimming artifact", a spurious migration of high-frequency energy toward the array due to the trade-off between the origin times of high-frequency sources and source-receiver distances.

To further reduce travel-time errors over the whole rupture, we apply the Slowness-Enhanced Back-Projection (SEBP) introduced by Meng et al. (2016). The conventional BP only requires knowledge of the hypocenter location and teleseismic travel times from the source region to the array stations. The latter are usually estimated assuming a 1-D reference velocity model (e.g. IASP91). The travel time errors due to 3D path effects result in a 'spatial bias' of the subevent locations imaged by BP. A "hypocenter correction" is routinely applied to mitigate travel time errors (Ishii et al., 2005, Ishii et al., 2007): travel time corrections for the hypocentral region are estimated by cross-correlation of initial P waveforms, then applied over the entire source region. However, the hypocenter correction is exact only in the immediate vicinity of the hypocenter, and its effectiveness decreases in more distant parts of large ruptures (Fan and Shearer, 2017; Meng et al., 2018). The SEBP method accounts for the spatial derivatives of travel-time in the source area through a slowness correction estimated from aftershock data. For a given aftershock, the differential travel-time between its BP-inferred location and its hypocenter is compared to predictions based on the 1D reference model. The difference is mapped into the slowness correction term.

We perform the SEBP on the high-frequency (0.5-2 Hz) P-wave seismograms recorded by 51 broadband stations of the Australian seismic network (AU). We first derived the slowness correction terms based on nine aftershocks with M ranging from 5.1 to 6.1 and quite evenly distributed across the mainshock rupture zone (Fig. 2 and Table S2). Their initial P waves have enough signal-to-noise ratio between 0.5 and 2 Hz at teleseismic distances. We relocate the aftershocks with respect to the mainshock hypocenter based on P-arrival times at regional

3

stations, so that the locations are accurate enough for a reliable slowness calibration (Table S2). Figure 2 compares the BP-imaged aftershock locations with and without the slowness correction. The initial BP locations (Fig. 2a) are generally biased northwestward with a root-mean-square error (RMSE) of 25.5 km. The bias is significantly reduced by our slowness calibration (Fig. 2b), down to a RMSE of 7.6 km. We then apply SEBP to the mainshock data. The epicenter is assumed to be located at [119.840°E, 0.178°S], as reported by National Earthquake Information Center (NEIC). Due to the limited depth sensitivity of BP, we back-project at a fixed depth of 10 km (the NEIC hypocenter depth).

We also assessed the rupture imaging potential of four other regional arrays in Alaska (AK), Japan (JP), New Zealand (NZ) and Turkey (EU) (Fig. S2). The JP and AK arrays are less satisfying due to unfavorable interference between P and pP phases. The NZ array, in a similar azimuth as AU, gives results overall consistent with those of the AU array but has poorer resolution due to its smaller azimuthal aperture. For the EU array, our SEBP resolved a similar rupture length and an overall supershear speed (Fig. S3).

The spatio-temporal characteristics of the kinematic rupture process are well imaged by SEBP (Fig. 1). The slowness calibration systematically shifts the BP locations towards the SSE direction, which is consistent with the pattern of aftershock corrections, and reveals a longer, and thus faster, rupture than what would be imaged without calibration (Fig. 2). The accuracy of the calibration is supported by the agreement between the rupture lengths determined by SEBP and by remote sensing. Coherent sources with significant beampower occur until approximately 45 s after rupture initiation (Fig. 1c). This source duration is consistent with the half-duration of 22.5 s reported by the routine USGS W-phase analysis. The HF sources follow an overall linear rupture path towards SSE, consistent with the surface fault traces identified by our SAR analysis (Fig. 1a). In two separate occasions, at around 10 s and 25 s, we observe more dispersed radiators, suggesting higher rupture complexity (Fig. 2b). The first episode of rupture perturbation coincides with the fault bend identified in the northern part of the rupture by the SAR analysis. The second episode roughly corresponds to the location of the Palu Bay, where the surface fault geometry is not visible from the SAR image. The southernmost part of the rupture, south of the large left bend, has much smaller amplitude radiators (Fig. 1).

Our SEBP reveals the Palu earthquake rupture was supershear. We estimate the rupture velocity based on least-square linear regression between the timing and the along-strike distance from the hypocenter of BP radiators in the first 45 s. We ignore the back propagating radiators around 30 s to prevent biasing low the rupture speed (Fig. 1d). The average rupture speed estimate and its standard deviation are $4.12 \pm 0.12 \, km/s$. The local shear-velocity ranges from 3.4 to 3.6 km/s between 3 and 20 km depth according to Crust 1.0 (https://igppweb.ucsd.edu/~gabi/rem.html). The rupture speed falls in between the local shear wave speed and the so-called Eshelby speed (sqrt(2)*Vs = 4.8~5.1 km/s). The supershear speed is sustained throughout the whole rupture, from the rupture onset to the end, as evidenced by the notable alignment of the radiators at the leading front in Figure 1d. Remarkably, supershear rupture persists despite the major bends of the surface rupture. Our BP analysis does not resolve an initial sub-shear rupture phase commonly observed in other supershear earthquakes.

Validation of supershear rupture with Rayleigh wave Mach cone

The supershear rupture speed indicated by BP analysis can be further validated by regional surface wave observations. The method was introduced by Vallée and Dunham (2012) and exploits the rupture directivity effect. For regular, sub-Rayleigh earthquakes, waves from different parts of the rupture arrive at a far-field receiver at different times. For supershear earthquakes, this is also the case outside the Mach cone, but on the Mach cone waves from different parts of the rupture arrive simultaneously. Along the Rayleigh wave Mach cone, but not elsewhere, the waveforms of a large supershear rupture should be identical to those of a smaller collocated event with similar focal mechanism, down to periods shorter than the rupture duration of the largest event and longer than its rise time. Their amplitude ratio should equal their seismic moment ratio. Such waveform similarities were first observed for the 2001 Kokoxili earthquake by Vallée and Dunham (2012).

We inspect the Rayleigh wave resemblance between the Palu mainshock and a smaller Mw 6.1 foreshock recorded by regional broadband stations near Indonesia and Australia. The smaller event is located 30 km south of the mainshock hypocenter and has a similar focal mechanism (Fig. 1a). Following Vallee and Dunham (2012) we filtered the Rayleigh waves in a narrow frequency band between 15 s and 25 s to minimize the dispersion effect. We consider stations at epicentral distances up to 45° (Fig. 3). In such a large region, the Rayleigh wave phase velocity c is heterogeneous. Taking into account the space- and frequency-dependent variability of the phase velocity estimated from the GDM52 model (Ekström, 2011), $\underline{c} = 3.30 \pm 0.1\ km/s$ for the southwest side of the Palu earthquake and $\underline{c} = 3.75 \pm 0.1\ km/s$ for the southeast side. The reliable value of the rupture velocity v_r resolved by SEBP, along with the acceptable values of phase velocity, empower us to predict the angle ϕ_M of the far-field Rayleigh Mach cone relative to the rupture propagation direction using the relation $\phi_M = arccos(c/v_r)$ (Vallée and Dunham, 2012) (Fig. 3). Nine stations are located on the eastern Rayleigh Mach cone, while only one is on the western cone due to the poor station coverage over the Indian Ocean.

Waveforms from the mainshock and the foreshock are extremely similar (correlation coefficients higher than 0.9) at the stations on the predicted Rayleigh Mach cone, but not at other azimuths (Figs. 3, 4, S5 and S6). The amplitude ratios on the Mach cone (125) are exactly equal to the theoretically expected value given by the moment ratio between the two events. This remarkable consistency supports the BP inference that the supershear speed was persistent from the beginning to the end of the mainshock rupture. Stations located further inside the Mach cone have smaller but still considerable similarities due to the directivity effect. Stations located outside the Mach cone, including in the direction opposite to the rupture, are the least similar. Taken all together, these results provide immediate evidence of a persistent supershear rupture velocity close to 4.1 km/s, which confirms our SEBP inferences.

Discussion

A key observation of the Palu earthquake, revealed here by SEBP and independently supported by analysis of the Rayleigh Mach cone, is its supershear rupture speed. Earlier evidence included the ratio between the rupture length estimated from the distribution of

aftershocks and the rupture duration from teleseismic source time functions, supported soon later by direct rupture length observations based on satellite images. Teleseismic source inversion properly constrains rupture duration but suffers from strong tradeoff between rupture size and rupture speed. A supershear rupture speed of 4.0 km/s was prescribed in the USGS National Earthquake Information Center teleseismic finite source inversion (https://earthquake.usgs.gov/earthquakes/eventpage/us1000h3p4/finite-fault) to match the rupture length inferred from satellite images. There is no local strong motion data available to study the near-field S-Mach wave of this event. The far-field surface wave Mach cone observations presented here are thus a highly valuable piece of evidence. Whether supershear rupture had an impact on the damage in Palu and the landslide triggering requires further scrutiny.

The Palu earthquake rupture is supershear from very early on. In theoretical models and laboratory experiments, the transition to supershear triggered by the daughter-crack mechanism occurs at a certain rupture propagation distance (Andrews 1976; Dunham, 2007; Xia et al., 2004). In that context, a short transition distance implies high initial shear stress on the fault or short critical slip-weakening distance. Early supershear can also be triggered by initial stress concentrations (Liu and Lapusta, 2008), which here could be due to the M6.1 foreshock or to fault roughness. Bouchon et al (2010) noted that supershear rupture happens on smooth faults. In dynamic models, rough faults promote the occurrence of *transient* supershear (Bruhat et al 2016). Yet, once triggered, this transient supershear can persist over longer distances if the rupture continues on a smoother section of the fault. Such interpretation would be consistent with the contrasting roughness of surface rupture in the northern and southern portions of the rupture revealed by remote sensing analysis. Despite such spatial variability of surface rupture geometry, the supershear speed of the Palu earthquake persists, quite steadily, over most of the rupture length. Alternatively, the fault could be smoother at depth than at the surface all along the rupture.

Yet the supershear Palu earthquake rupture is not as fast as P waves. It is even slower than the Eshelby speed, which is the lower end of stable supershear speeds in dynamic rupture models (Burridge et al. 1979; Rosakis et al., 1999). Steady rupture at a nominally unstable supershear speed can result from interactions between dynamic rupture and head waves in a low-velocity damaged fault zone (Huang et al., 2015). In that context, the Palu earthquake could correspond to a stable supershear rupture at the P wave speed of a fault damage zone with 30% reduction of wave speed relative to the host rock. Such level of rock damage is not uncommon in mature fault zones (e.g., Huang et al., 2014), although it is unclear it extends across the whole seismogenic depth. The Palu-Koro fault has an accumulated slip of the order of 200 km, large enough to have developed a mature damage zone. Damaged fault zones also tend to shorten the supershear transition distance (Huang et al., 2015), which makes this interpretation appealing to explain also the early onset of supershear in the Palu earthquake.

The observation of early and persistent supershear is enabled here primarily by teleseismic back-projection with aftershock-based slowness calibration. The Palu earthquake highlights the technological improvement of earthquake source imaging through SEBP. As demonstrated also in BP studies of the 2015 M 7.8 Gorkha earthquake (Meng et al., 2016) and the M 8.3 Illapel earthquake (Meng et al., 2018), the slowness correction effectively reduces the spatial bias of BP. Our confidence on the SEBP results comes from the consistency between multiple arrays and the remarkable agreement between the rupture path inferred from satellite

images. Such agreement was first achieved for the 2013 Mw 7.7 Balochistan earthquake (Avouac et al., 2014). Real-time automated BP has been proposed to complement earthquake and tsunami early warning (Meng et al., 2014; An and Meng, 2016) and rapid ground-motion estimations (Feng and Meng, 2018). The slowness correction pre-determined with background earthquakes is an important consideration for such applications.

Acknowledgements

References

An, C., & Meng, L. (2016). Application of array backprojection to tsunami prediction and early warning. *Geophysical Research Letters*, *43*(8), 3677-3685.

Andrews, D. J. (1976). Rupture velocity of plane strain shear cracks. *Journal of Geophysical Research*, *81*(32), 5679-5687.

Avouac, J. P., Ayoub, F., Wei, S., Ampuero, J. P., Meng, L., Leprince, S., ... & Helmberger, D. (2014). The 2013, Mw 7.7 Balochistan earthquake, energetic strike-slip reactivation of a thrust fault. *Earth and Planetary Science Letters*, *391*, 128-134.

Bouchon, M., Karabulut, H., Bouin, M. P., Schmittbuhl, J., Vallée, M., Archuleta, R., ... & Marsan, D. (2010). Faulting characteristics of supershear earthquakes. *Tectonophysics*, *493*(3-4), 244-253.

Bruhat, L., Fang, Z., & Dunham, E. M. (2016). Rupture complexity and the supershear transition on rough faults. *Journal of Geophysical Research: Solid Earth*, *121*(1), 210-224.

Burridge, R. (1973). Admissible speeds for plane-strain self-similar shear cracks with friction but lacking cohesion. *Geophysical Journal of the Royal Astronomical Society*, *35*(4), 439-455.

Burridge, R., Conn, G. & Freund, L. B. The stability of a rapid mode II shear crack with finite cohesive traction. J. Geophys. Res. 85, 2210-2222 (1979).

Das, S. (2015). Supershear Earthquake Ruptures–Theory, Methods, Laboratory Experiments and Fault Superhighways: An Update. In *Perspectives on European Earthquake Engineering and Seismology* (pp. 1-20). Springer, Cham.

Dunham, E. M. (2007). Conditions governing the occurrence of supershear ruptures under slip-weakening friction. *Journal of Geophysical Research: Solid Earth*, *112*(B7).

Fan, W., & Shearer, P. M. (2017). Investigation of backprojection uncertainties with M6 earthquakes. *Journal of Geophysical Research: Solid Earth*, *122*(10), 7966-7986.

Feng, T., & Meng, L. (2018). A High-frequency Distance Metric in Ground-Motion Prediction Equations Based on Seismic Array Back-Projections. *Geophysical Research Letters*.

Y. Huang, J. P. Ampuero and D. V. Helmberger (2015) The potential for supershear earthquakes in damaged fault zones - Theory and observations *Earth Planet. Sci. Lett., 433*, 109-115, doi:10.1016/j.epsl.2015.10.046

Huang, Y., Ampuero, J.-P. & Helmberger, D. V. Earthquake ruptures modulated by waves in damaged fault zones. J. Geophys. Res., 119, 3133–3154, doi:10.1002/2013JB010724 (2014).

Ishii, M., Shearer, P. M., Houston, H., & Vidale, J. E. (2005). Extent, duration and speed of the 2004 Sumatra–Andaman earthquake imaged by the Hi-Net array. *Nature*, *435*(7044), 933.

Ishii, M., Shearer, P. M., Houston, H., & Vidale, J. E. (2007). Teleseismic P wave imaging of the 26 December 2004 Sumatra-Andaman and 28 March 2005 Sumatra earthquake ruptures using the Hi-net array. *Journal of Geophysical Research: Solid Earth*, *112*(B11).

Kiser, E., & Ishii, M. (2017). Back-projection imaging of earthquakes. *Annual Review of Earth and Planetary Sciences*, *45*, 271-299.

Liang, C., and E. J. Fielding (2017), Interferometry With ALOS-2 Full-Aperture ScanSAR Data, *IEEE Transactions on Geoscience and Remote Sensing*, *55*(5), 2739-2750, doi:10.1109/TGRS.2017.2653190.

Liu, Y. & Lapusta, N. Transition of model II cracks from sub-Rayleigh to intersonic speeds in the presence of favorable heterogeneity. J. Mech. Phys. Solids 56, 25-50 (2008).

Meng, L., Inbal, A., & Ampuero, J. P. (2011). A window into the complexity of the dynamic rupture of the 2011 Mw 9 Tohoku-Oki earthquake. *Geophysical Research Letters*, *38*(7).

Meng, L., Ampuero, J. P., Stock, J., Duputel, Z., Luo, Y., & Tsai, V. C. (2012). Earthquake in a maze: Compressional rupture branching during the 2012 Mw 8.6 Sumatra earthquake. *Science*, *337*(6095), 724-726.

Meng, L., Zhang, A., & Yagi, Y. (2016). Improving back projection imaging with a novel physics-based aftershock calibration approach: A case study of the 2015 Gorkha earthquake. *Geophysical Research Letters*, *43*(2), 628-636.

Meng, L., Bao, H., Huang, H., Zhang, A., Bloore, A., & Liu, Z. (2018). Double pincer movement: Encircling rupture splitting during the 2015 Mw 8.3 Illapel earthquake. *Earth and Planetary Science Letters*, *495*, 164-173.

Pathier, E., E. Fielding, T. Wright, R. Walker, B. Parsons, and S. Hensley (2006), Displacement field and slip distribution of the 2005 Kashmir earthquake from SAR imagery, *Geophysical Research Letters*, *33*(20), doi:10.1029/2006GL027193.

Perrin, C., Manighetti, I., Ampuero, J. P., Cappa, F., & Gaudemer, Y. (2016). Location of largest earthquake slip and fast rupture controlled by along-strike change in fault structural maturity due to fault growth. *Journal of Geophysical Research: Solid Earth*, *121*(5), 3666-3685.

Rosakis, A. J., Samudrala, O. & Coker, C. Cracks faster than the shear wave speed. Science 284, 1337-1340 (1999).

Rosen, P. A., E. Gurrola, G. F. Sacco, and H. Zebker (2012), The InSAR Scientific Computing Environment, paper presented at 9th European Conference on Synthetic Aperture Radar, Nuremberg, Germany, 23-26 April.

Socquet, A., Vigny, C., Chamot-Rooke, N., Simons, W., Rangin, C., & Ambrosius, B. (2006). India and Sunda plates motion and deformation along their boundary in Myanmar determined by GPS. *Journal of Geophysical Research: Solid Earth*, *111*(B5).

Vallée, M., & Dunham, E. M. (2012). Observation of far-field Mach waves generated by the 2001 Kokoxili supershear earthquake. *Geophysical Research Letters*, *39*(5).

Watkinson, I. M., & Hall, R. (2017). Fault systems of the eastern Indonesian triple junction: evaluation of Quaternary activity and implications for seismic hazards. *Geological Society, London, Special Publications*, *441*(1), 71-120.

Xia, K., Rosakis, A. J., & Kanamori, H. (2004). Laboratory earthquakes: The sub-Rayleigh-to-supershear rupture transition. *Science*, *303*(5665), 1859-1861.
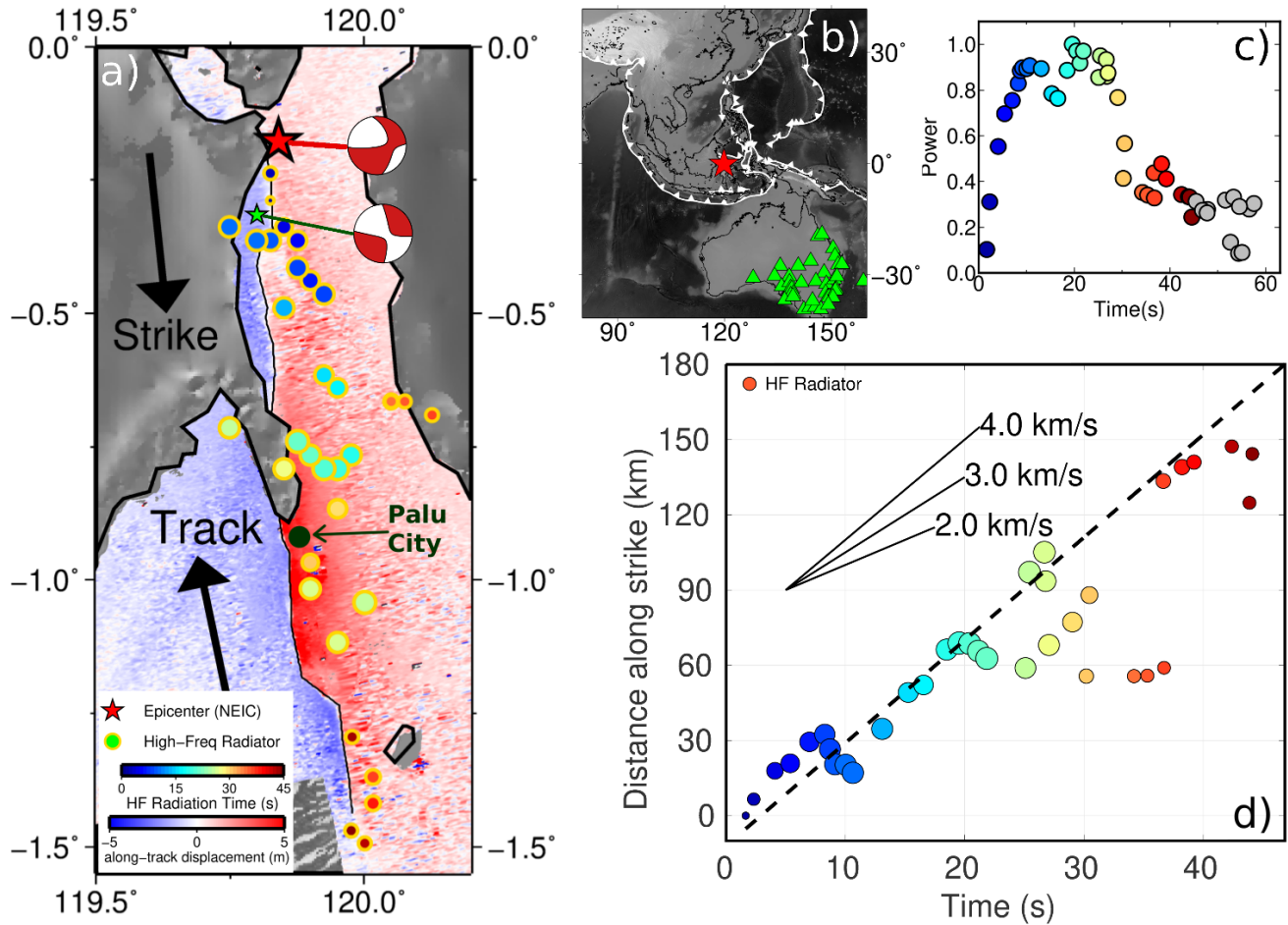
Figure 1. Surface rupture trace and supershear speed of the Palu earthquake. **a)** Along-track displacements from ALOS-2 SAR offsets (colored image on land) and bathymetry (gray background offshore). The arrow labeled as "track" indicates the direction of measurement, -11.7°. The red star denotes the NEIC epicenter of the Palu earthquake. The green star is the relocated epicenter of the 2018/09/28 M6.1 foreshock. Mainshock and foreshock focal mechanisms are also shown. The inferred surface rupture trace is indicated by a thin black line. Circles are the high-frequency (0.5~2 Hz) radiators imaged by the Slowness-Enhanced Back-Projection (SEBP) on data recorded by the Australia array, with size proportional to relative energy and color representing rupture time with respect to the mainshock origin time. **b)** Map showing the mainshock epicenter (red star) and stations of the Australia array used for SEBP (green triangles). **c)** Beam power as a function of time. Low-amplitude radiators after 45 seconds (gray) are not used in further analysis. **d)** Along-strike location and timing of radiators imaged by SEBP. Time is relative to rupture origin time. Location is the horizontal position relative to the hypocenter, projected along the average strike direction (174°). The solid lines indicate reference rupture speeds. The dashed line is a linear regression of the leading front radiators.
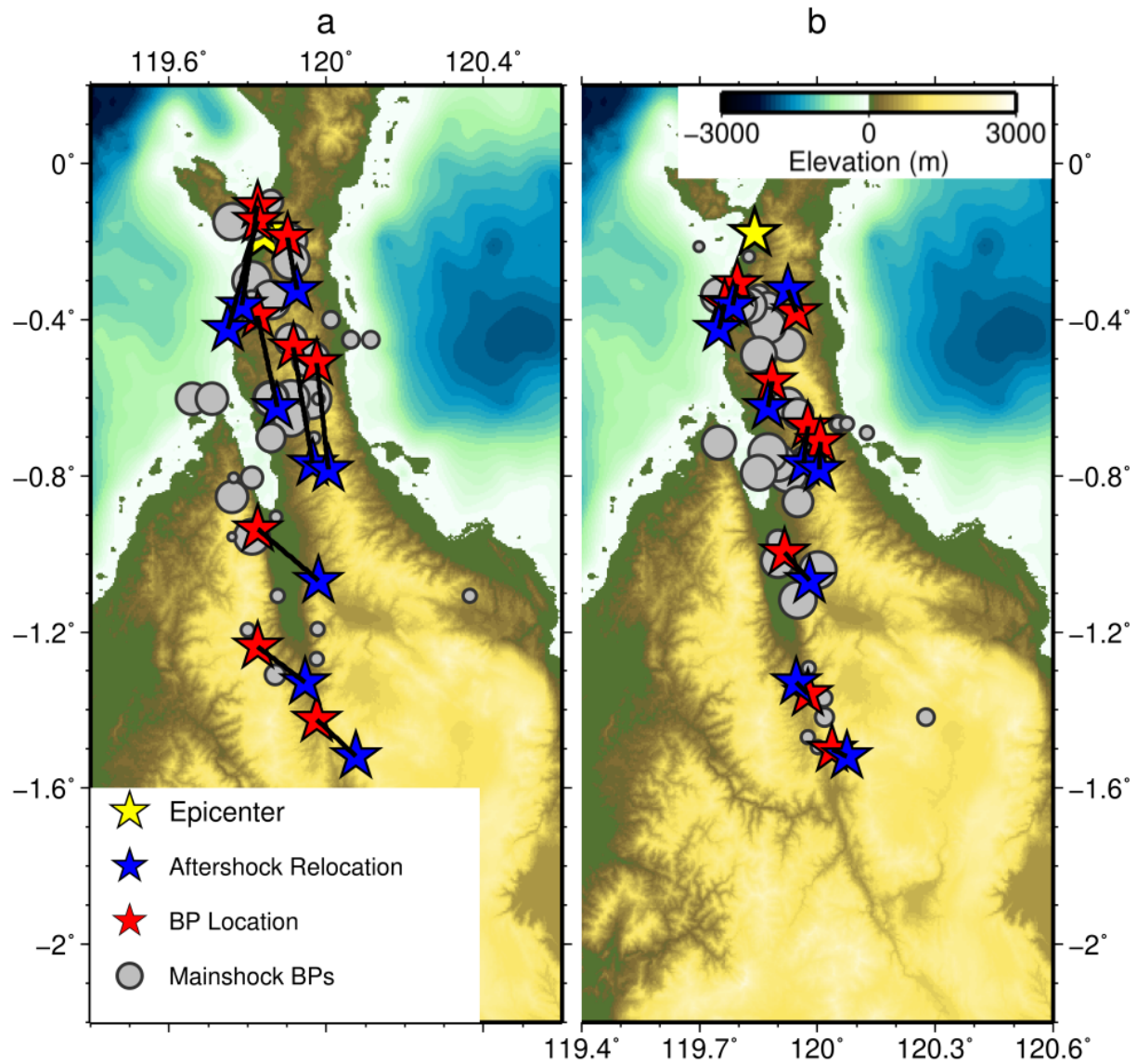
Figure 2. Calibration of back-projection based on aftershock data. BP-inferred (red stars) and relocated (blue stars) locations of 9 M5.1+ aftershocks spanning the rupture region, and BP radiators (gray circles) before (a) and after (b) the slowness calibration. Results shown are for Australia array.
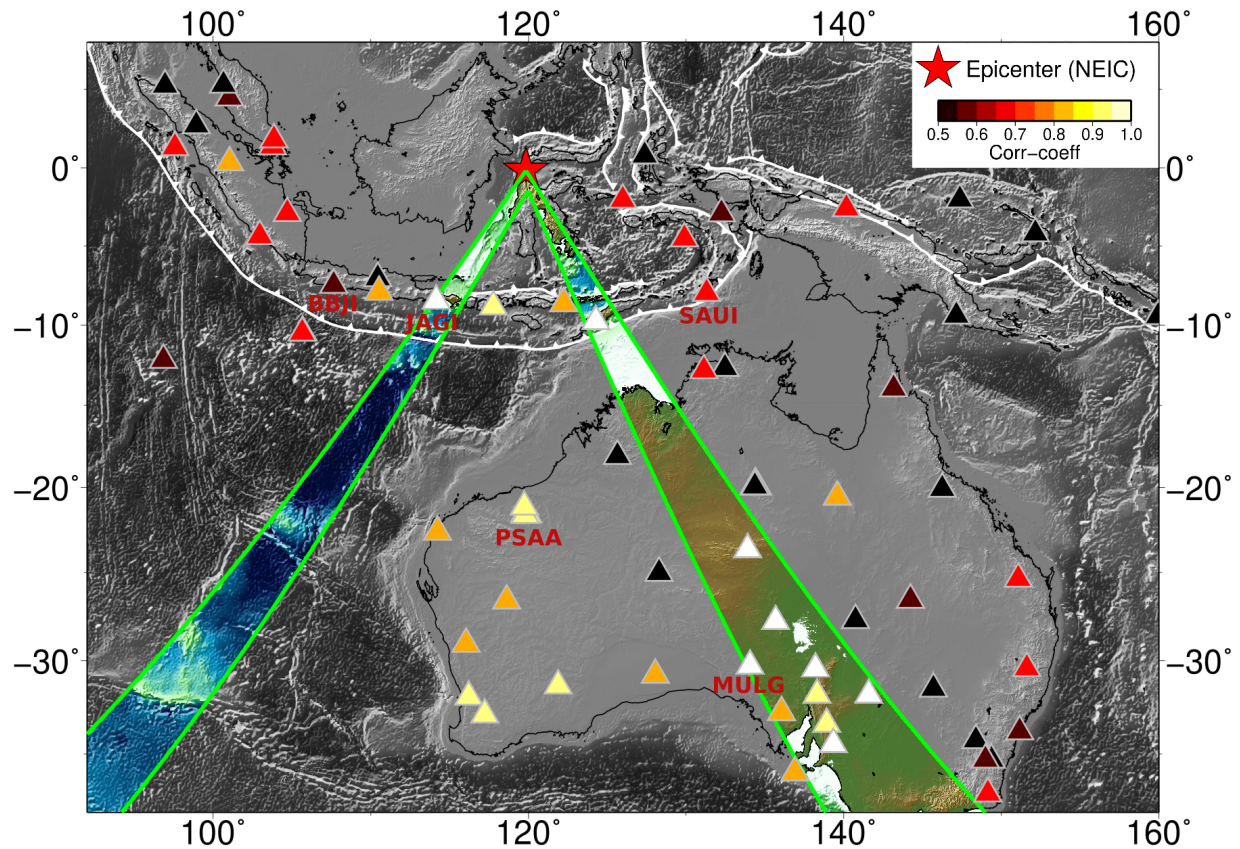
Figure 3. Evidence of a far-field Rayleigh-wave Mach cone. The colored area inside the green lines is the predicted area scanned by the Mach cone, based on the observed rupture velocity (4.1 km/s) and uncertainties in Rayleigh wave phase velocity. The location of broadband stations are indicated by triangles. Their color indicates correlation coefficients between 15–25 s Rayleigh wave displacement seismograms of the Palu earthquake and its M6.1 foreshock.
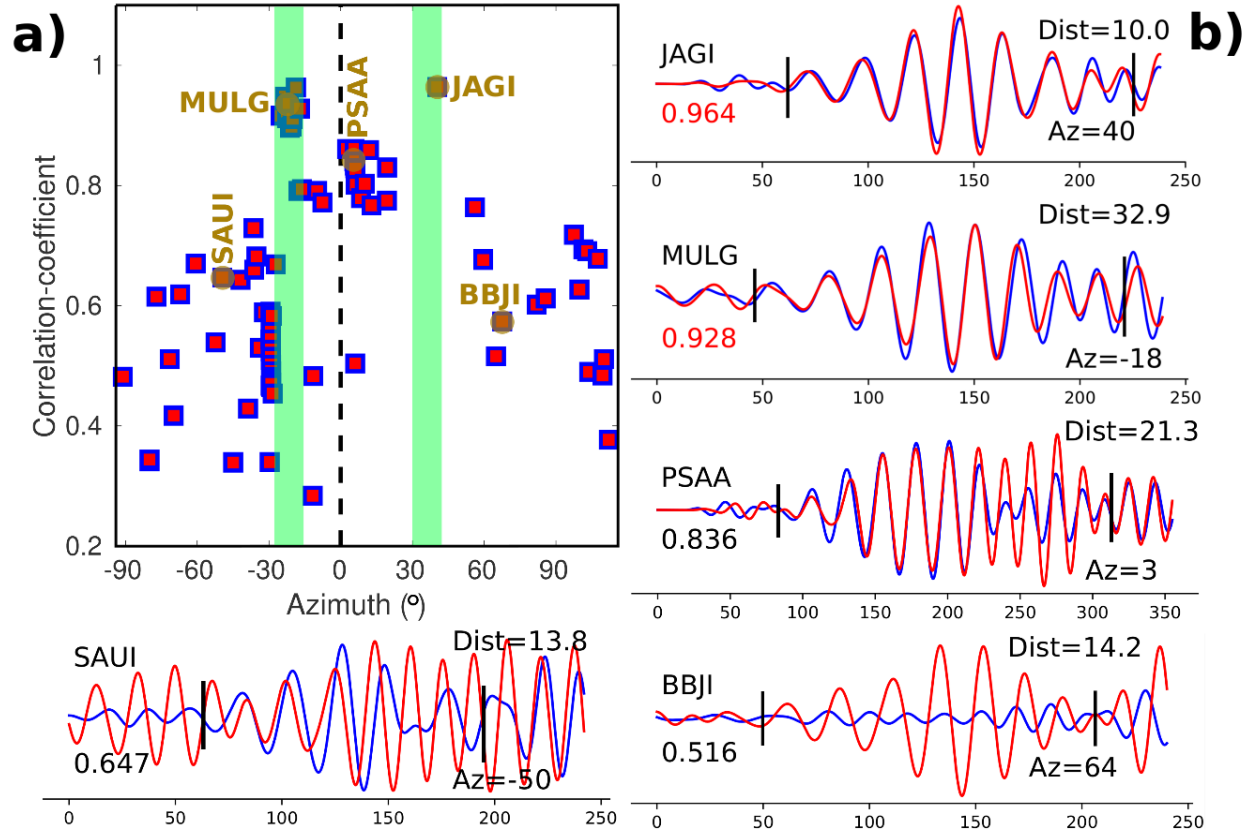
Figure 4. Evidence of Rayleigh Mach waves. **a)** Correlation coefficients (red squares) between 15~25 s Rayleigh waves of the mainshock and its M 6.1 foreshock (see Fig. 1a) as a function of stations azimuth relative to the rupture strike. The dashed line indicates the fault strike direction. The two green-colored bands indicate the estimated azimuth ranges of the two Mach cones, considering uncertainties in Rayleigh wave phase velocity and rupture velocity. The correlation coefficients reach the highest values at stations on the predicted Mach cone. **b)** Rayleigh wave vertical displacement seismograms of mainshock (blue) and foreshock (red) in the 15–25 s period range. Station name, azimuth (Az) relative to the rupture direction, and hypocentral distance (Dist) are shown for each station. Values of the normalized cross-correlation coefficient, based on the signal windows between the two vertical ticks, are shown in red for stations on Mach cones. Foreshock signals are scaled by the mainshock/foreshock moment ratio, 125. Names of the four chosen stations are marked in both Figure 2 and Figure 4a.
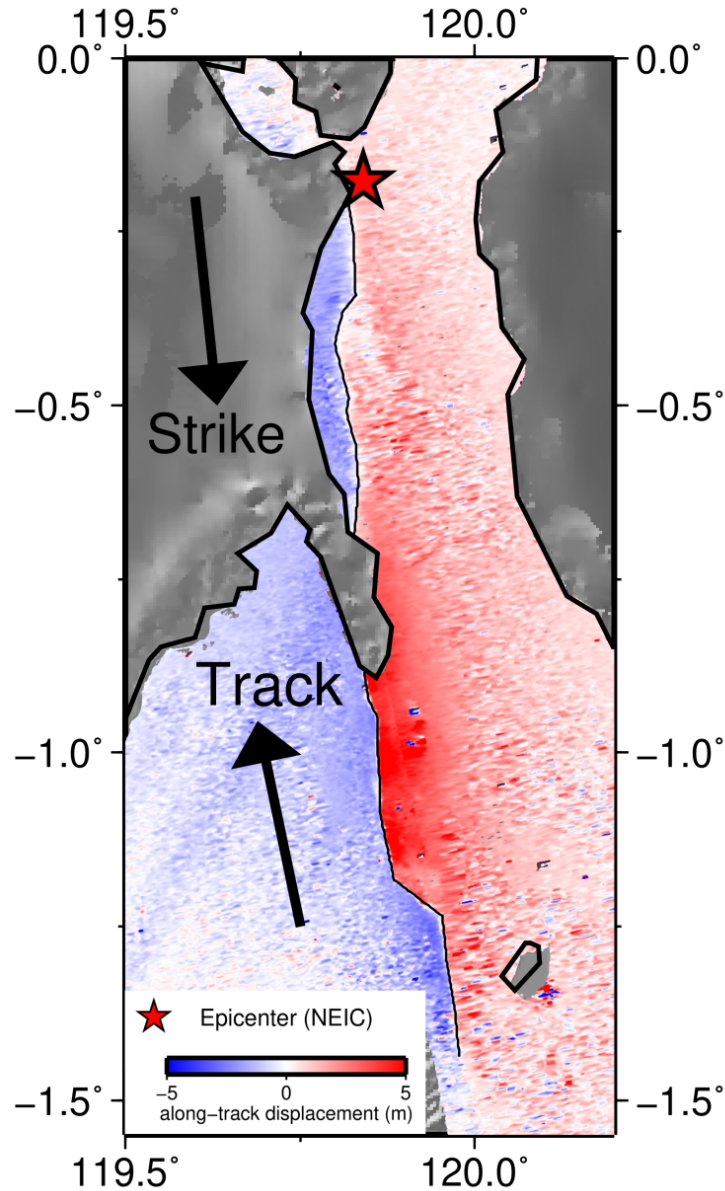
Figure S1. High-resolution along-track displacements from ALOS-2 SAR offsets (colored image on land) and bathymetry (gray background offshore). The arrow labeled as "track" indicates the direction of the measurement, -11.7°. The red star denotes the NEIC epicenter of the Palu earthquake. This is the same as figure 1a but plotted without the back-projection results, to show without obstruction the interpretation of the surface rupture trace from the SAR results.

ALOS-2 path	date1	date2	frames	beam
127	2018/08/08	2018/10/03	7160–7170	SM3 F2-7
126	2018/08/17	2018/10/12	7150–7190	SM3 F2-5

Table S1. JAXA ALOS-2 PALSAR-2 scenes used in the pixel offset analysis.

AU array	Magnitude	Relocated locations		BP location		BP location with Calibration	
		lat	lon	lat	lon	lat	lon
2018-09-28 08:24:58	5.0	-0.363	119.785	-0.107	119.825	-0.309	119.795
2018-09-28 07:00:01	6.1	-0.423	119.750	-0.147	119.825	-0.359	119.764
2018-09-28 12:27:33	5.1	-0.323	119.925	-0.188	119.901	-0.381	119.946
2018-10-01 23:46:39	5.2	-0.623	119.875	-0.390	119.825	-0.557	119.885
2018-09-28 10:50:25	5.7	-0.768	119.965	-0.471	119.916	-0.673	119.976
2018-09-28 10:16:49	5.7	-0.783	120.005	-0.511	119.976	-0.713	120.007
2018-09-28 10:25:04	5.8	-1.0681	119.980	-0.936	119.825	-0.996	119.916
2018-09-28 13:39:44	5.2	-1.328	119.945	-1.238	119.825	-1.358	119.976
2018-09-28 11:06:51	5.2	-1.518	120.075	-1.425	119.976	-1.501	120.037
2018-09-28 10:47:44	5.1	Low signal coherence					
2018-09-28 10:39:03	5.4	Relocation error too large (>20km)					

Table S2. Locations of two foreshocks and all (M>5.1) aftershocks in the vicinity of the mainshock rupture region (by Oct 08, 2018). The first 9 events are used in the slowness calibration of the back-projection (AU array). The root-mean-square (RMS) error between the BP locations and the relocated aftershock locations is reduced from 25.5 km to 7.6 km by the slowness calibration.
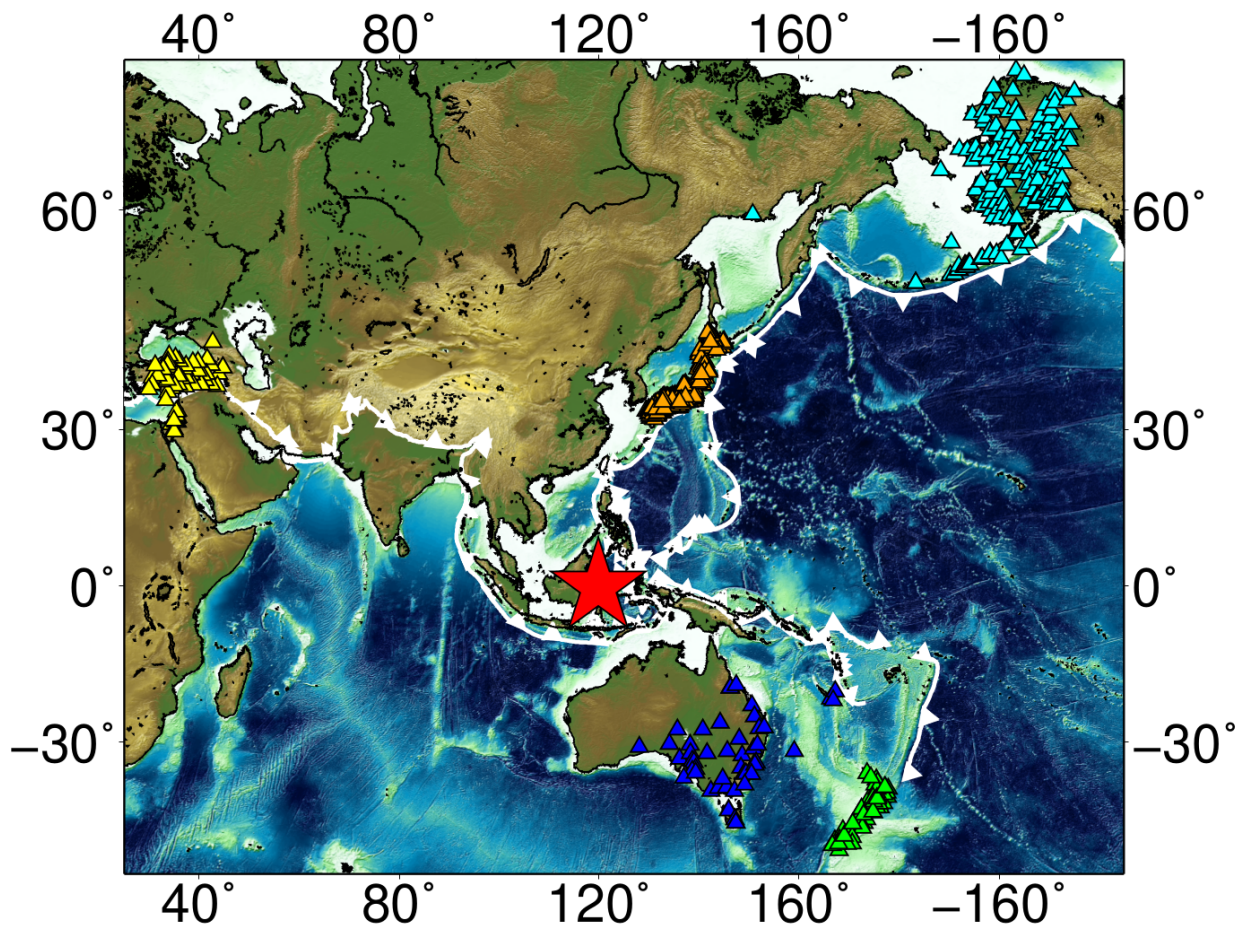
Figure S2. Teleseismic arrays considered for the back-projection analysis. The colored triangles represent the seismic stations from arrays in Turkey (yellow), Australia (blue), New Zealand (green), Japan (orange), and Alaska (cyan). The red star denotes the location of the Mw7.5 Palu earthquake.
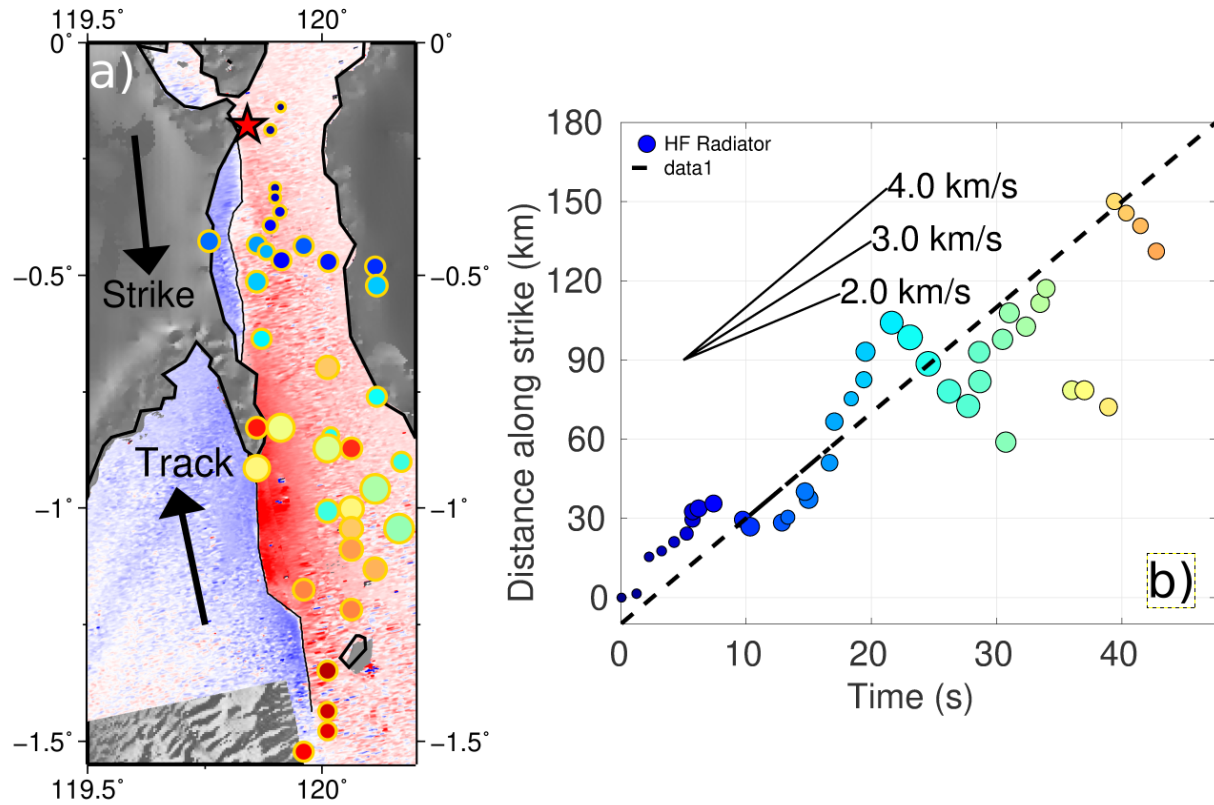
Supplementary Materials

Figure S3. Rupture imaging by Slowness-Enhanced Back-Projection (SEBP) of data recorded by the Turkish array. **a)** Circles denote the high-frequency (0.5~2 Hz) radiators, with size proportional to relative energy (beamforming power) and color representing rupture time with respect to the mainshock origin time. Note that the spatial bias along the west-east direction on the southern part of the rupture is not perfectly corrected by our aftershock calibration (see Figure S4). **b)** Along-strike location and timing of radiators. Time is relative to rupture origin time. Location is the horizontal position relative to the hypocenter, projected along the average strike direction (174°). The solid lines indicate reference rupture speeds. The dashed line is a linear regression of the leading front radiators. The average rupture speed estimate and its standard deviation are $4.08 \pm 0.16 \; km/s$.
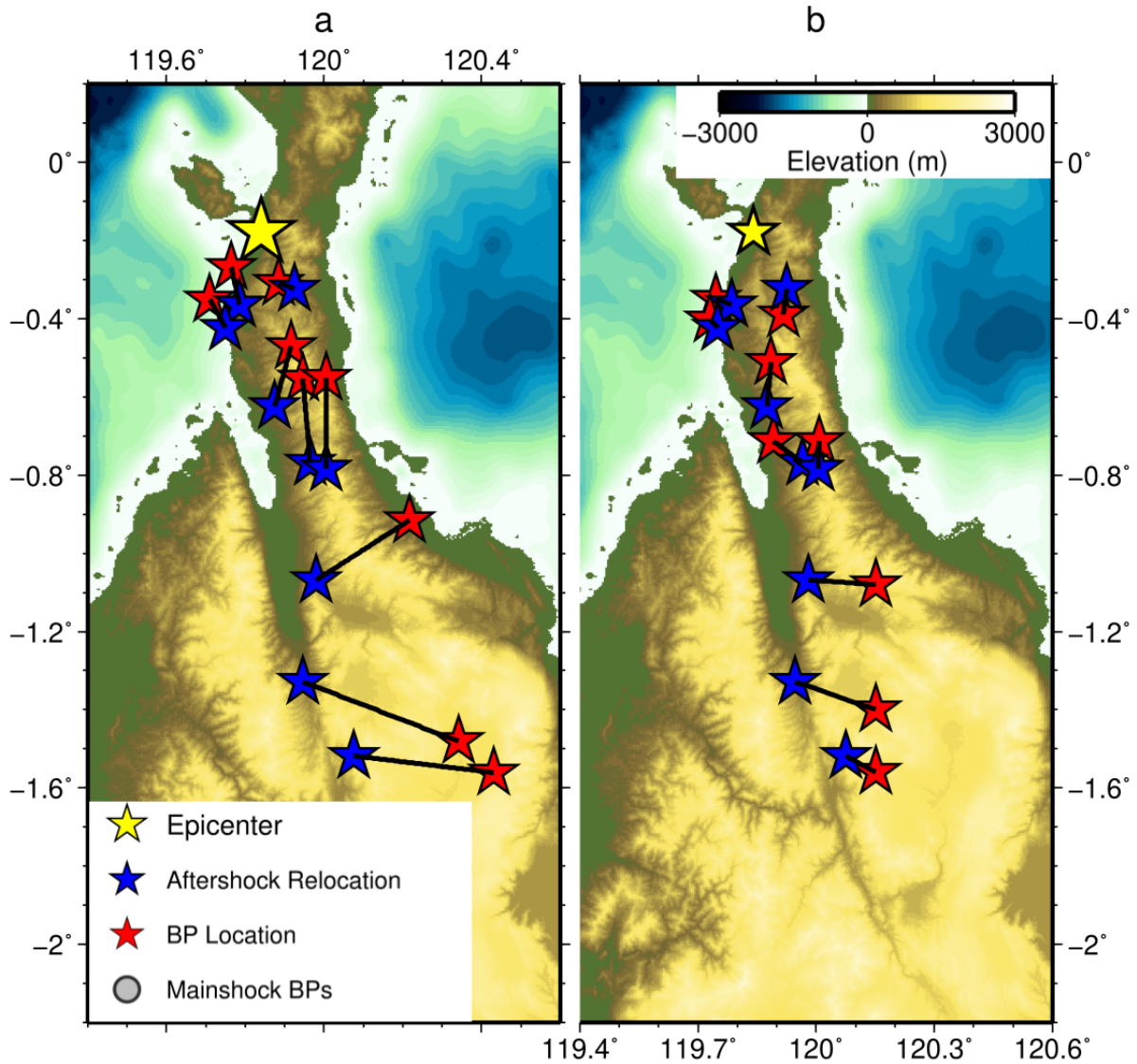
Figure S4. Slowness calibration of back-projection based on aftershock data for the Turkish array. BP-inferred (red stars) and relocated (blue stars) locations of 9 M5.1+ aftershocks spanning the rupture region, before (a) and after (b) the slowness calibration. The root-mean-square error (RMSE) is decreased by slowness calibration from 27.1 km to 12.4 km.

EU array	Magnitude	Relocated locations		BP location		BP location with Calibration	
		lat	lon	lat	lon	lat	lon
2018-09-28 08:24:58	5.0	-0.363	119.785	-0.267	119.764	-0.349	119.744
2018-09-28 07:00:01	6.1	-0.423	119.750	-0.350	119.710	-0.401	119.731
2018-09-28 12:27:33	5.1	-0.323	119.925	-0.309	119.885	-0.390	119.916
2018-10-01 23:46:39	5.2	-0.623	119.875	-0.471	119.916	-0.511	119.885
2018-09-28 10:50:25	5.7	-0.768	119.965	-0.553	119.946	-0.713	119.891
2018-09-28 10:16:49	5.7	-0.783	120.005	-0.552	120.006	-0.713	120.007
2018-09-28 10:25:04	5.8	-1.0681	119.980	-0.915	120.218	-1.077	120.152
2018-09-28 13:39:44	5.2	-1.328	119.945	-1.481	120.341	-1.359	120.151
2018-09-28 11:06:51	5.2	-1.518	120.075	-1.561	120.431	-1.560	120.150
2018-09-28 10:47:44	5.1	Low signal coherence					
2018-09-28 10:39:03	5.4	Relocation error too large (>20km)					

Table S3. Locations of two foreshocks and all aftershocks in the vicinity of the mainshock rupture region (by Oct 08, 2018). The first 9 events are used in the slowness calibration of the back-projection (Turkish array). The root-mean-square (RMS) error between the BP locations and the relocated locations is reduced from 27.1 km to 12.4 km.
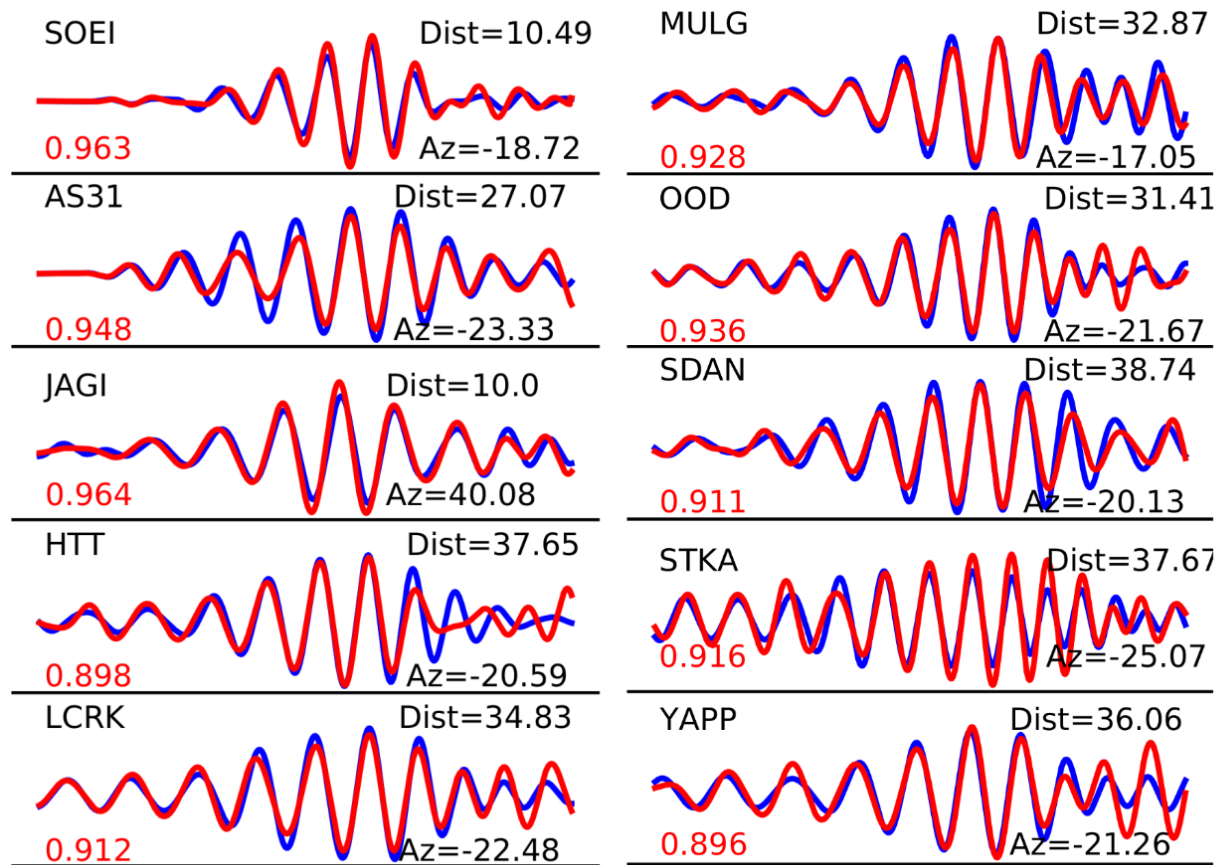
Figure S5. Rayleigh wave vertical displacement seismograms of mainshock (blue) and foreshock (red) in the 15–25 s period range recorded at stations located in Mach cones. Station name, azimuth relative to the rupture direction (Az), hypocentral distance (Dist), and correlation coefficient (red) are shown for each station.
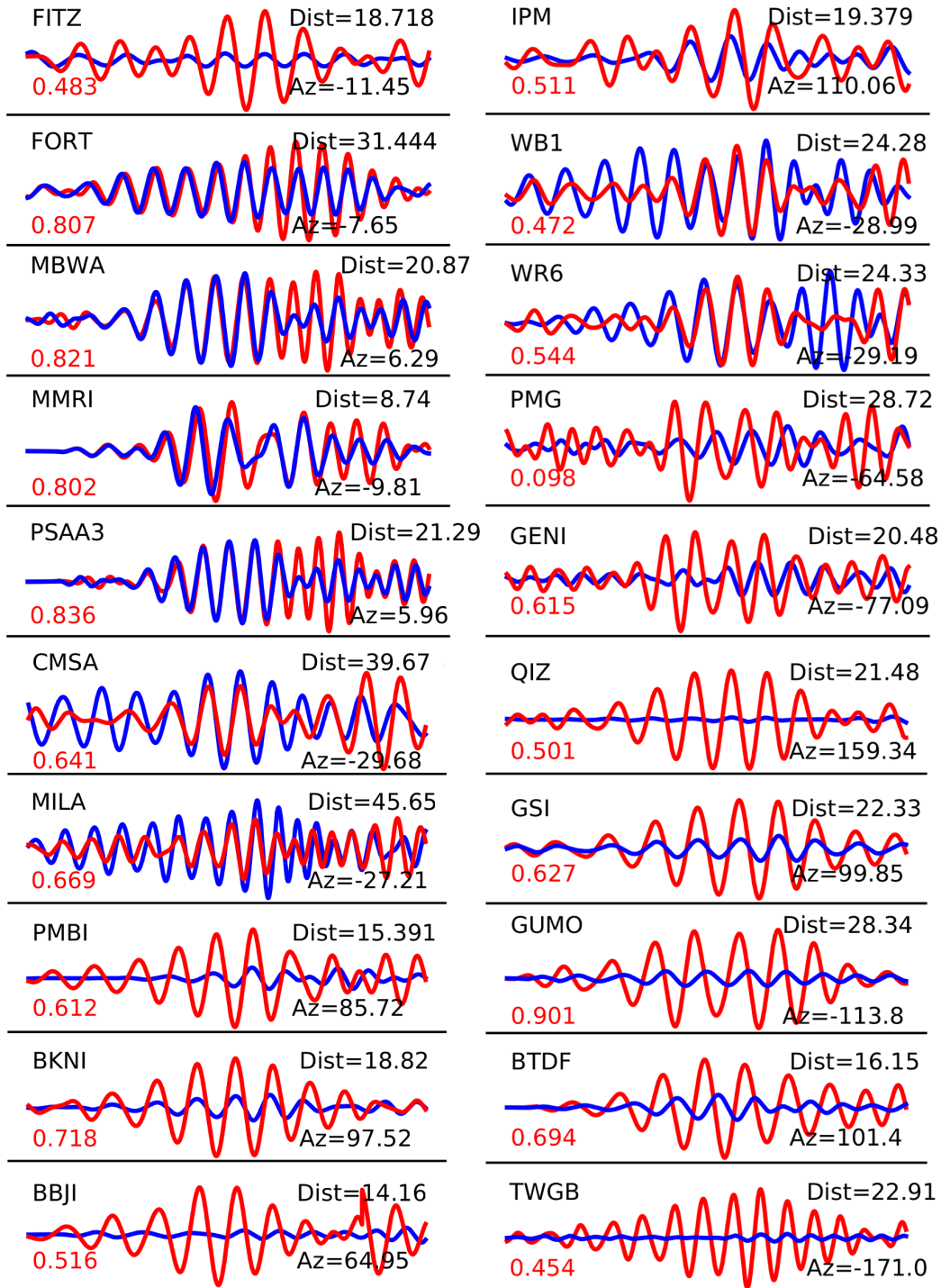
Figure S6. Rayleigh wave displacement seismograms of mainshock (blue) and foreshock (red) in the 15–25 s period range recorded at stations located out of Mach cones. Station name, azimuth (Az) relative to the rupture direction, hypocentral distance (Dist), and correlation coefficient (red decimal) are shown for each station.